

# Structure, composition, and chemical reactivity of carbon nanotubes by selective nitrogen doping

Stephen Maldonado, Stephen Morin, Keith J. Stevenson \*

*Department of Chemistry and Biochemistry, Center for Nano- and Molecular Science and Technology, Texas Materials Institute, The University of Texas at Austin, Austin, TX 78712, United States*

Received 5 July 2005; accepted 28 November 2005  
Available online 19 January 2006

## Abstract

Carbon nanotubes (CNTs) doped with a range of nitrogen contents (0–10 at.%) were prepared via a floating catalyst CVD method using ferrocene, NH<sub>3</sub>, and xylene or pyridine. XPS and Raman microscopy were used to assess quantitatively the compositional and structural properties of the nitrogen-doped carbon nanotubes (N-CNTs). XPS analysis indicates a shift in and broadening of the C 1s spectra track with increasing disorder induced by selective nitrogen doping. N 1s XPS spectra show three principle types of nitrogen coordination (pyridinic, pyrrolic, and quaternary), with the pyridinic-like fraction selectively increased from 0.0 to 4.5 at.%. First-order Raman spectra were fit with five peaks that vary in intensity and width with nitrogen content. The ratio of the D and G bands' integrated intensities scaled linearly with nitrogen content. Iodimetric titrations were used to gauge the number of reducing sites on as-prepared N-CNTs, representing the first report of nitrogen doping as a means to deterministically effect the chemical reactivities of carbon nanotubes. The reported methodology for the regulated growth and selective nitrogen doping of CNTs presents new ways to study systematically the influence of nanocarbon composition and structure on chemical and electrochemical reactivity for a host of applications. © 2005 Elsevier Ltd. All rights reserved.

*Keywords:* Carbon nanotubes; Carbon nanofibers; Doping; Catalytic properties; Interfacial properties

## 1. Introduction

Heteroatom doping (e.g., boron, sulfur, phosphorous, and nitrogen) of graphitic carbon lattices effects various physicochemical properties of sp<sup>2</sup> carbon materials [1,2]. In particular, the substitutional doping of nitrogen has received focused attention because significant changes in hardness, electrical conductivity, and chemical reactivity have been theoretically predicted and experimentally observed [3–5]. Several methods for preparation of nitrogen doped carbon materials have been used including sputter deposition [6], graphitization of nitrogen-containing polymers [7], and exposure of pre-formed carbons at elevated temperatures to reactive gases (HCN and NH<sub>3</sub>) [8,9]. While the former two routes typically produce mate-

rials useful as inert coatings [6] and adsorbents [9,10], respectively, the latter route has been particularly promising for the preparation of activated carbons that demonstrate enhanced chemical reactivity for electron transfer processes [8,11–13], including those important to battery and fuel cell applications [14,15]. Although many studies have evaluated structure-composition-property relationships of these N-doped carbons, the influence of nitrogen doping on resultant physicochemical properties has not been fully delineated [8,14]. For example, carbon surface areas, surface functionalities, and degree of graphitization vary strongly with the different carbon materials used and their pretreatment and processing histories. Further, the nitrogen doping process is a complex function of the activation conditions employed (e.g., reactant gas concentration, reaction time, temperature). As such, many diverse and sometimes conflicting conclusions have been made about N-doped carbons [16].

\* Corresponding author. Fax: +1 512 471 8696.  
E-mail address: [stevenson@mail.cm.utexas.edu](mailto:stevenson@mail.cm.utexas.edu) (K.J. Stevenson).

An attractive alternative that enables the direct growth and substitutional nitrogen doping of nanocarbons involves the use of gas phase precursors rather than the liquid or solid precursors commonly employed for typical “classic” carbon production [17–20]. Gas phase nanocarbon synthesis via chemical vapor deposition (CVD) techniques offers exceptional promise for regulated control of physicochemical properties such as heteroatom doping, crystallinity, and degree of exposed edge plane sites [21–31]. Previous reports from our laboratory have described the influence of nitrogen doping on CNT electrodes for oxygen reduction [28,32], hydrogen peroxide decomposition [32], and catechol oxidation reactions [33]. Herein, we present results that describe the controlled growth and selective nitrogen doping of carbon nanotubes prepared through a modified floating catalyst method [34] using pyridine and  $\text{NH}_3$ . Prior reports of selective nitrogen doping of CNTs through  $\text{NH}_3$  and a pure carbon source like ethylene or xylene have demonstrated only a narrow range of nitrogen doping ( $\Delta\text{N} \sim 2$  at.%) with a maximum nitrogen content of  $\approx 2.5$  at.% [29,35]. Our method reports on the use of  $\text{NH}_3$  coupled with a carbon–nitrogen source involving pyridine to enable the regulated growth of CNTs containing nitrogen from 4 up to 10 at.%. This provides for a more direct basis for establishing correlations between the chemical and electrochemical reactivity of carbon and its structure, texture, and composition. XPS, Raman and iodometric titrimetry were performed to establish correlations between nitrogen content, nitrogen-binding configuration, CNT composition, structure and chemical reactivity.

## 2. Experimental

### 2.1. CNT preparation

Ferrocene (99%, Aldrich) was used as received as the growth catalyst. CNT and N-CNTs made without  $\text{NH}_3$  were prepared via a floating catalyst CVD process using the same dual heated zone system and a similar methodology as reported earlier [32]. For N-CNTs made with  $\text{NH}_3$ , freshly distilled and dried pyridine (Aldrich) was used as the carbon source. An integrated and automated system consisting of programmable syringe pumps (New Era Pump Systems NE-1000), electronic gas mass flow controllers (MKS Type 1479A), and two single-zone tube furnaces (Carbolite Model HST 12/35/200/2416CG) interfaced through a single computer running a customized LabVIEW program was used. Solutions consisting of  $20 \text{ mg ml}^{-1}$  of ferrocene in pyridine were loaded into 1.0 ml gas tight glass syringes (Hamilton 81320). The syringes were interfaced with stainless steel lines that fed into the center of the front half of an air tight quartz tube (26 mm OD, 22 mm ID) located in furnace 1. The quartz tube spanned the two tube furnaces. After a 15 min Ar (Praxair, 99.997%) purge at 200 sccm of the quartz tube, furnace 2 was heated to 800 °C. Following a 5 min thermal equilibra-

tion period, furnace 1 was heated to 130 °C. Concurrently,  $\text{NH}_3$  (99.99%, Aldrich) and Ar gas flows were raised to a total carrier gas flow of 575 sccm. Various ratios of  $\text{NH}_3$  and Ar gases were used, but a total flow of 575 sccm was consistent for all trials. 1 ml of the ferrocene solution was fed into furnace 1 at a rate of  $0.1 \text{ ml s}^{-1}$  for a total of 10 min. Once completed, furnaces 1 and 2 were allowed to cool under 200 sccm Ar. For all conditions, the floating catalyst CVD methodology resulted in thick, dark films of CNTs coating the interior of the quartz tube and the top of silicon wafers with 100-nm-thick oxide layers located in furnace 1. Collected materials were stored in individual air tight vials prior to characterization.

### 2.2. TEM analysis

Transmission electron microscopic (TEM) analysis of the CNTs was performed with a JEOL 2010F operating at 200 kV. Prior to analysis, the CNTs were dispersed in methanol and then drop cast onto a Cu TEM grid covered with a thin amorphous carbon film.

### 2.3. XPS analysis

X-ray photoelectron spectroscopy was conducted with a PHI 5700 ESCA system possessing a scan step size of 0.1 eV and an Al  $\text{K}\alpha$  monochromatic line (1486.6 eV), calibrated with the signals for Au 4f<sub>7/2</sub>, Ag 3d<sub>5/2</sub>, and Cu 2p<sub>3/2</sub>. The C 1s spectra were collected with a single scan. N 1s spectra were scan averaged five times. Atomic percentages were determined from elemental survey scans and are reported relative to the total signals for carbon, nitrogen, and iron. Spectra were analyzed using a freeware software package, FITT 1.2 (Photoelectron Spectroscopy Lab, Seoul National University) with Shirley background corrections.

### 2.4. TGA analysis

Thermal gravimetric analysis (TGA) data were collected with a TA Instruments Q500. Sample sizes of 1–5 mg of N-CNTs were loaded into platinum pans and heated to 900 °C in flowing air (Praxair, 99.998%) with a  $60 \text{ ml min}^{-1}$  flow rate to the sample and a  $40 \text{ ml min}^{-1}$  flow rate of  $\text{N}_2$  (Praxair, 99.998%) to the balance.

### 2.5. Raman analysis

Spectra were obtained with a Renishaw inVia system, using a 514.5 nm Ar laser at  $3 \text{ mW cm}^{-2}$  and a 50× aperture (NA = 0.75) resulting in approximately a 2  $\mu\text{m}$  diameter sampling cross section. Spectra were acquired in a single scan with an acquisition time of 500 s. Raw spectra were fit with GRAMS/AI 7.02® software by the Levenberg–Marquadt method [36] using 5 bands located at 1624, 1583, 1487, 1351, and  $1220 \text{ cm}^{-1}$ , denoted as D', G, D'', D, and I, respectively, according to the convention

of Cuesta et al. [37]. A linear baseline correction was used for all spectra to compensate for the photoluminescence background. All spectral fits had correlation factor ( $R^2$ ) values greater than 0.998.

## 2.6. Iodimetric analysis

Iodimetric analysis was conducted as described by Oliveira et al. [38]. Dried  $K_2Cr_2O_7$  (Fisher, 99.98%),  $Na_2S_2O_3$  (99.8%, Fisher), and starch indicator (99.6%, MCB reagents) were dissolved in NANOpure® (18 M $\Omega$  cm, Barnstead) water.  $I_2$  (99.8%, Fisher) was dissolved with excess NaI to generate  $I_3^-$ . The  $Na_2S_2O_3$  and  $I_3^-$  solutions were stored in covered containers to avoid light exposure. 0.1 M  $Na_2S_2O_3$  solutions were standardized with 0.05 M  $K_2Cr_2O_7$  and NaI (99.7%, Baker) and then used to standardize the 0.05 M  $I_3^-$  solution. 10 ml of  $I_3^-$  solution and 20 mg of either non-doped CNTs or N-CNTs were combined in a clean 25 ml round bottom flask with a stir bar. The flask was then sealed with a septum, mounted onto a stirrer, covered completely with aluminum foil, purged with  $N_2$  (99.999%, Praxair), and vigorously stirred for 24 h. Following, the CNT suspension was filtered into a clean Erlenmeyer flask through a 60 ml medium porosity glass frit filter. Approximately 90 ml of NANOpure water were used to rinse off solution from the CNTs. The excess  $I_3^-$  filtrate was back titrated with  $Na_2S_2O_3$  until a golden yellow color was observed. 800  $\mu$ l of starch indicator were added, rendering the solution a deep blue hue. Further  $Na_2S_2O_3$  was added until the solution became clear, denoting the endpoint. Measurements were done in triplicate.

## 3. Results and discussion

### 3.1. CNT growth observations

As reported previously [32], nitrogen doping by this preparation route does not drastically change the gross morphology (length, diameter) of the obtained carbon nanotubes. Transmission electron microscopy (TEM) analysis shows that both non-doped and N-doped CNT diameters remained nominally constant (15–40 nm) and verified that carbon nanotubes were the sole product under CVD growth conditions (Fig. 1). We note that CNT length and diameter slightly decreases (10–20%) with increasing fraction of  $NH_3$  in the carrier gas. Nominal lengths are  $\sim 10 \mu$ m. In addition, we demonstrated that the solvent in the CVD process determines the elemental composition of CNTs in the absence of  $NH_3$  gas, where xylene solvents yield non-doped CNTs while pyridine solvents result in nitrogen doping at consistent levels of  $4.0 \pm 0.5$  at.% [32]. The addition of  $NH_3$  to pyridine-containing CNT synthesis allows greater control of the nitrogen content, as seen in Fig. 2. Increasing the  $NH_3$  fraction in the carrier gas stream in the presence of pyridine yielded a linear increase ( $0.43 \pm 0.03$  at.% N per %  $NH_3$ ) in the nitrogen doping of the N-CNTs, with contents up to  $\sim 10$  at.% when the

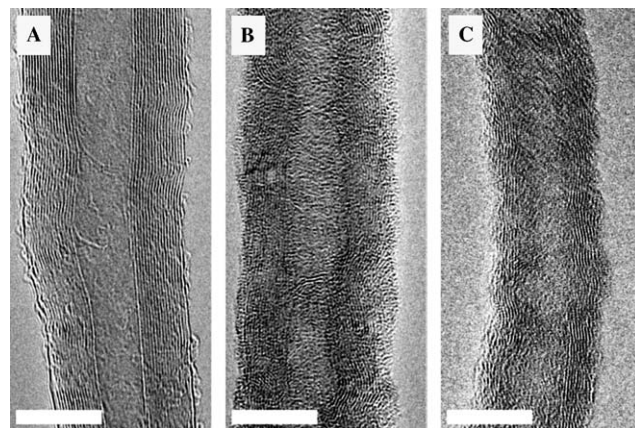


Fig. 1. Representative transmission electron micrographs of (A) non-doped CNTs, (B) N-CNTs ( $5.1 \pm 0.5$  at.%), and (C) N-CNTs ( $9.6 \pm 0.5$  at.%) prepared by floating catalyst CVD. Scale bars: 10 nm.

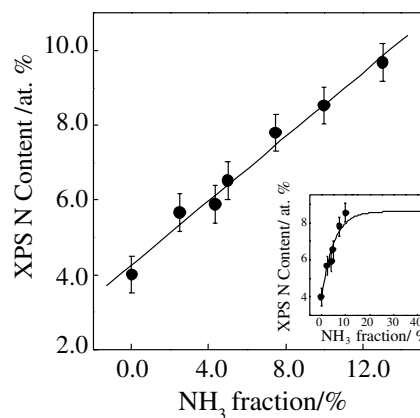


Fig. 2. Nitrogen content in the CNTs as a function of  $NH_3$  carrier gas fraction as measured by XPS for CNTs prepared from mixtures containing ferrocene, pyridine, and  $NH_3$ .

$NH_3$  feed stream fraction was less than 14%. Fig. 2 also shows the sensitivity of the total nitrogen content with varying fractional amount of  $NH_3$  at a constant temperature, highlighting the advantage of in-situ transition metal-catalyzed graphitization and doping of carbon.  $NH_3$  feed stream fractions above 15% showed no additional influence on increasing nitrogen content; rather, slightly depressed nitrogen doping levels are seen (inset of Fig. 2), presumably due to increased gasification of carbon at high  $NH_3$  concentration. Similar trends of the influence of  $NH_3$  levels on nitrogen doping have been noted by Jang et al. [29], Kim et al. [35], and Lee et al. [39]. At elevated temperatures, decomposition of  $NH_3$  in the presence of carbon-containing materials generates free radical species, e.g.,  $NH_2^{\cdot}$  [11]. At low levels the produced radical species presumably facilitate nitrogen incorporation into the CNT graphitic structure, but at high levels these radicals attack graphitic carbon and hasten its gasification to methane and cyanogen species.

Fig. 3 demonstrates that increases in the fractional amount of  $NH_3$  in the carrier gas results in the increase

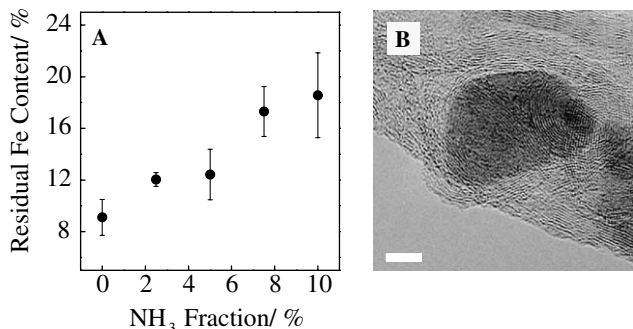


Fig. 3. (A) Residual iron (wt.%) in CNTs as a function of NH<sub>3</sub> carrier gas fraction as measured by TGA for CNTs prepared from mixtures containing ferrocene, pyridine, and NH<sub>3</sub>. (B) Representative TEM image of residual iron catalysts. Scale bar: 5 nm.

of relative amounts of residual iron in the N-CNTs. As shown in Fig. 3B, TEM analysis indicated that iron particles were located within the interior as well as the exterior of the CNTs and typically encapsulated with layers of graphene [32]. Assuming that the total number of iron particles generated from the decomposition of ferrocene is roughly independent of carrier gas composition, the relative proportion of residual iron in the CNTs increased with NH<sub>3</sub> fraction because of increased gasification of graphitic carbon. This is consistent with reports from Lee et al. [26] that describe an inhibitory effect of high NH<sub>3</sub> levels on CNT growth rates for a similar CVD-based methodology. Hence, high fractions of NH<sub>3</sub> in the carrier gas (>15%) were determined to be detrimental to CNT production and studies reported herein are limited to N-CNTs produced using NH<sub>3</sub> carrier gas composition below this level.

### 3.2. XPS analysis

Fig. 4 shows representative C 1s spectra for CNTs doped with increasing amounts of nitrogen. The peak position at 284.4 eV for CNTs with 0.0 at.% nitrogen is very close to the accepted value (284.3 eV) for pure sp<sup>2</sup> C–C

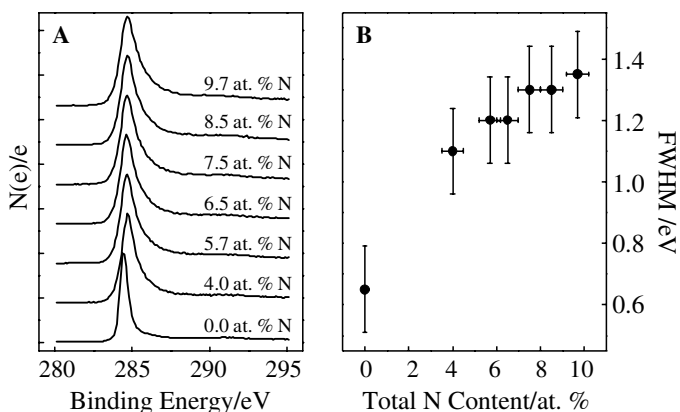


Fig. 4. (A) Normalized XPS C 1s spectra (single scan) of CNTs with increasing nitrogen content. (B) Full width at half maximum (FWHM) of the C 1s spectra in (A) as a function of nitrogen content.

bonding in pristine highly oriented pyrolytic graphite (HOPG) [40], indicating carbon atoms are almost exclusively sp<sup>2</sup> hybridized in non-doped CNTs. The peak positions for all N-CNTs in Fig. 4A are shifted to 284.7 eV. Any subtle differences in the peak positions of the various N-CNTs exceeded the resolution of the XPS instrument. This 0.3 eV shift for N-CNTs is consistent with previously reported values for nitrogenated thin carbon films [41] and is in agreement with increased structural disorder, i.e., more disruptions in the sp<sup>2</sup> carbon framework from the incorporation of nitrogen within the graphene lattice [32,33]. While a small, broad band centered near 291 eV is present in all CNT spectra (Fig. 4A) no discernible side bands commensurate with extensive oxygen-like functionalities (e.g., quinones, carboxyl groups) are visible in the 286–289 eV shoulder region [42,43]. The band located at 291 eV is assigned to the  $\pi$ – $\pi^*$  interband, a common feature in graphitic carbon XPS spectra which does not strongly correlate with structural disorder [44]. However, the signal at 284 eV does broaden and become slightly more asymmetric with increasing nitrogen content. The FWHM values for the peak in Fig. 4A are plotted against the respective nitrogen doping levels in Fig. 4B. The FWHM for CNTs with 0.0 at.% nitrogen is very close to the reported 0.6 eV FWHM value for HOPG [45] and is also indicative of non-doped sp<sup>2</sup> carbon, while the FWHM values for N-CNTs increase with additional nitrogen content. There are several possible sources for the observed broadening and asymmetry in the spectra for N-CNTs. Since core-hole screening in conductive materials unavoidably imparts line asymmetry in XPS spectra [44–46], the increased asymmetry of the C 1s peak of N-CNTs may denote a change in the excitation spectrum of the conduction electrons, i.e., the electronic density of states. Terrones et al. [47] have demonstrated an increase in the population of states in the electronic band gap of N-CNTs produces carbons with more metallic/conductive character. However, asymmetry and broadening of the peak in C 1s spectra have also been attributed to a sideband at 285.6 eV arising from lattice disorder, i.e., sp<sup>3</sup> bonding character [44]. For a series of semi-coke materials with negligible heteroatom content, the intensity and contribution of this “defect” band was shown to scale with increasing structural disorder. Further, there are several contradictory reports of C 1s bands associated with C–N functionalities in the 285–286 eV region, complicated by strong band overlap in this range that prevents definitive band assignment(s) [41,48–50]. Although contributions from the aforementioned sources to the peak in the C 1s spectra are hard to differentiate, the observed changes in Fig. 4 are nevertheless indicative of doping-induced changes in the electronic, structural, and bonding character of the N-CNTs.

High resolution N 1s XPS spectra were obtained to elucidate more fully the identity of nitrogen coordination in the N-CNTs. Fig. 5 demonstrates representative N 1s spectra for CNTs doped with varied nitrogen levels. For all NH<sub>3</sub>-derived N-CNTs, the N 1s spectra in Fig. 5A exhibit

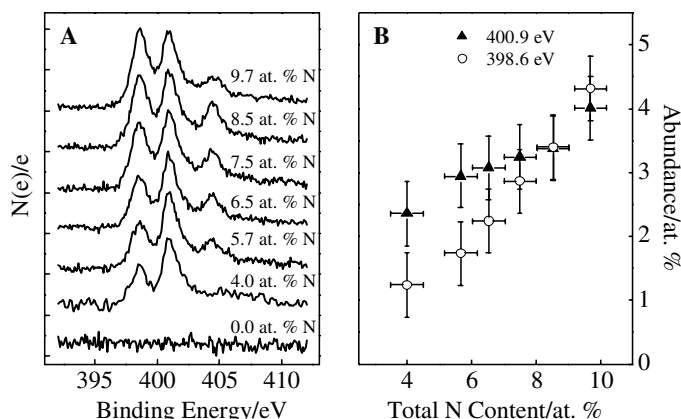


Fig. 5. (A) Normalized XPS N 1s spectra (5 scan averaged) of CNTs with increasing nitrogen content. (B) Relative abundances of the peaks at 400.9 and 398.6 eV obtained from the spectra in (A).

three strong, distinct peaks at 398.6, 400.9, and 404.2 eV. Assignment of the latter peak is unclear, as several authors have reported peaks at 402.9–403.2 eV for pyridine-N-oxide functionalities [51,52], at 404.9–405.6 eV for chemisorbed nitrogen oxide [53], at 403.9 eV for physisorbed  $N_2$  [54,55], and at 402–404.2 eV for  $\pi$ - $\pi^*$  shake-up satellites [7,56]. Designation of the 404.2 eV bands as pyridine-N-oxide or physisorbed nitrogen oxide necessitates an excessively large shift of  $\sim 1$  eV, which is particularly unlikely given the peak's sharp and well-defined shape in Fig. 5A. Assignment as either a  $\pi$ - $\pi^*$  shake-up satellite or physisorbed  $N_2$  more accurately fits the experimental peak positions. N 1s shake-up satellites have been reported with moderate intensity [53] but typically when identified they are very broad [53,56]. Formation of  $N_2$  during the pyrolytic formation/doping of the CNTs is plausible and binding of  $N_2$  to the CNT surface may comment on the sorptive nature of the carbon. However, physisorbed  $N_2$  is typically not observed on graphite unless pre-cleaned surfaces are strongly dosed with  $N_2$  at low temperatures [55]. Although specific assignment is not made to the peak at 402.2 eV, it is most likely not due to incorporated nitrogen. Regardless, since this is not a predominant peak we focus our main attention on peaks near 400 eV. A large number of C–N functionalities have been assigned to the region near 400 eV [8,25,51,52]. Typically, for carbon nitride materials, the N 1s spectra contains two very broad peaks that overlap considerably, a consequence of either a heterogeneous spatial distribution [57] of the functionalities arising from extensively disordered  $sp^3$  carbon framework or to the overlap of several closely spaced bands resulting from numerous C–N functionalities [50,58,59]. The sharpness of the peaks in Fig. 5A imply that the nitrogen atoms of the N-CNTs are homogeneously dispersed and that the distribution of possible C–N functionalities is narrow. The peak at 398.6 eV was fitted with a single Lorentzian band which correlates well with binding energies reported by Boehm et al. [8] and Pels et al. [51] for pyridinic functionalities decorating the surface of  $NH_3$ -treated activated car-

bons. The peak at 400.9 eV was also fitted with two Lorentzian bands at 400.4 and 401.4 eV, suggestive of pyrrolic-like and quaternary-like nitrogen coordination, respectively [51]. The relative intensities of the two bands at 399 and 400 eV in the N 1s spectra change with increasing levels of incorporated nitrogen. Fig. 5B displays the relative abundances of these two peaks as a function of total nitrogen content in the N-CNTs. While both peaks increase in abundance with higher total nitrogen doping, the pyridinic peak (398.6 eV) shows a twofold greater rise in abundance ( $0.24 \pm 0.01$  at.% per %  $NH_3$ ) than the pyrrolic/quaternary (400.9 eV) peak ( $0.11 \pm 0.01$  at.% per %  $NH_3$ ). This twofold increase in relative abundance suggests that doping via  $NH_3$  results in a selective bias for nitrogen coordination as pyridinic-like functionalities.

### 3.3. Raman analysis

Fig. 6 shows representative first-order Raman spectra for CNTs containing 0.0 and 9.7 at.% nitrogen. Two maxima are apparent in both spectra, occurring near 1355 and 1585  $cm^{-1}$ . A dramatic broadening of the two peaks for N-CNTs is visible in Fig. 6B relative to Fig. 6A, as reported previously [32,33] and elsewhere [60]. In addition, two other spectral features become more pronounced with nitrogen doping. First, overlap between the two signals at 1355 and 1585  $cm^{-1}$  in Fig. 6B becomes so great that the direct measurement of distinct FWHM values is not possible. Second, asymmetric tailing of the peak at 1355  $cm^{-1}$  results in a shoulder with measurable intensity extended out to  $\sim 1000$   $cm^{-1}$  for N-CNTs containing 9.7 at.% nitrogen nearly 300  $cm^{-1}$  farther than the corresponding tailing for non-doped CNTs. Simple line broadening does not account for these phenomena, as both spectra in Fig. 6 cannot be deconvoluted into just two Lorentzian or Gaussian shapes. Cuesta et al. [37], Angoni [57], and Darmstadt et al.

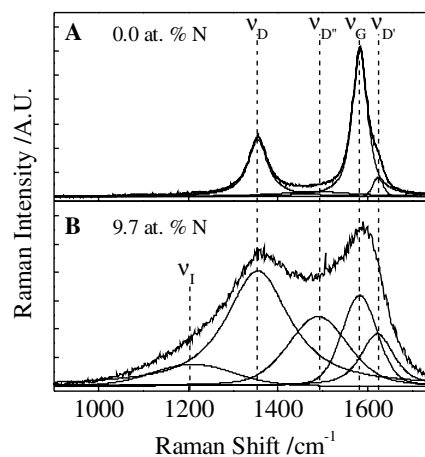


Fig. 6. Comparison of peak intensities and widths used in the fitting of the first-order Raman spectra for CNTs containing (A) 0.0 at.% and (B) 9.7 at.% N.

[61] similarly noted that several bands were necessary to fit the Raman spectra of polycrystalline graphitic materials. Accordingly, five bands at 1624, 1583, 1487, 1355, and 1220  $\text{cm}^{-1}$  referred to as D', G, D'', D, and I, respectively, following the convention of Cuesta et al. [37] and Bonhomme et al. [62], were used for fitting. For both Fig. 6A and B, the G and D bands are the most intense spectral features. The G band arises from a  $E_{2g}$  vibrational mode in the  $D_{6h}^4$  symmetry group of graphite crystal planes and is seen for all  $sp^2$  carbon Raman spectra [63]. There is less consensus for the origin of the D band, but it is generally accepted as a Raman inactive mode (e.g.,  $A_{1g}$ ) that becomes active from a reduction in symmetry at or near crystalline edges [64] and is subsequently used as an indicator of edge plane density. The D' and D'' bands differ in relative intensity between Fig. 6A and B. For CNTs with 0.0 at.% nitrogen in Fig. 6A, the two bands are visible, but are minor constituents in the overall shape of the spectrum. In contrast, for N-CNTs (Fig. 6B), the D' and D'' bands are very intense and significantly contribute to the shape of the curve. Although the sources of the D' and D'' bands are unclear [37], the D' band has been attributed to irregular  $d_{002}$  spacing [1] while the D'' band has also tentatively been designated as an indicator of defects in graphene layer stacking [65]. Interestingly, both the D' and D'' bands occur at Raman shifts near or at peaks in the phonon density of states for graphite [63] that are predicted to be Raman inactive but, like the D band, may become active due to relaxations in local symmetry arising from lattice distortions [64]. The increases in D' and D'' band generally suggest a larger turbostratic character in graphene plane stacking, i.e., loss of coherent  $d_{002}$ , in nitrogen doped carbons as predicted by Sjoström et al. [6], and is in agreement with a previous TEM observation [32]. The occurrence of the I band is the most striking difference between Fig. 6A and B, as the I band is not at all apparent in the spectrum for CNTs, but is strong enough to give the broad shoulder in the N-CNTs Raman spectra. The I band has been observed in moderately to heavily disordered graphitic carbons [37,57]. Angoni [57] has ascribed the I band to impurities in the graphite lattice, but it was not observed in the first-order Raman spectra of boron-doped graphite [64]. As with the D' and D'' bands, a relaxation in symmetry from a  $sp^2$  lattice distortion may allow a Raman inactive peak in the predicted density of phonon states  $\sim 1220 \text{ cm}^{-1}$  [64] to be Raman active. However, since the I band is not visible in Raman spectra for non-doped CNTs, the specific type of lattice distortion causing the relaxation of symmetry may be distinct from the structural distortions responsible for the D, D', and D'' bands, i.e., not specifically edge plane density or turbostratic character. Hence, while the I band may not be a direct consequence of nitrogen doping, the corresponding symmetry breaks may be directly a result of the incorporation of nitrogen and so the I band in this case reports on its presence. As shown in Fig. 6B, the correlation of the I band to nitrogen doping is further supported by the entirely Gaussian nature of the

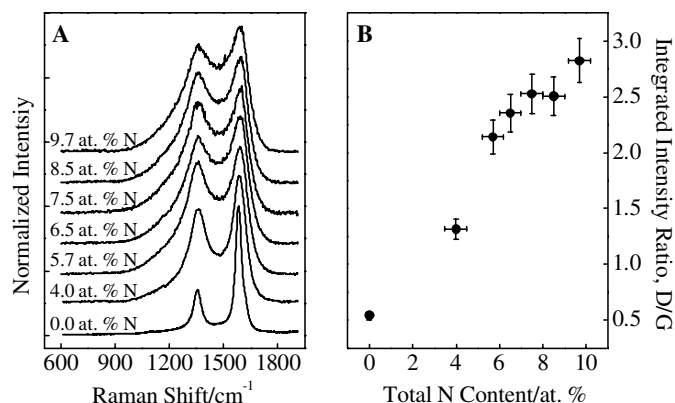


Fig. 7. (A) Normalized and baseline corrected first-order Raman spectra of CNTs with increasing nitrogen content. (B) Ratio of the integrated intensities for D and G bands (as in Fig. 5) as a function of nitrogen content.

peak shape (<1% Lorentzian character). Heterogeneous distributions of spectroscopically active elements produce Gaussian line shapes in the corresponding spectroscopic signatures [57]. The Gaussian shape of the I band agrees qualitatively with the observance of a heterogeneous distribution of nitrogen atoms, consistent with the multiple nitrogen functionalities indicated by XPS.

The first-order Raman spectra for N-CNTs with increasing nitrogen content are presented in Fig. 7. The spectra in Fig. 7A are all normalized to the intensity of the latter peak, but a decrease in the absolute magnitude of the Raman signal with increasing nitrogen doping was observed, evidenced by the decrease in signal-to-noise of the spectra for N-CNTs with higher nitrogen contents for identical acquisition conditions. Applying the assignments of Fig. 6 to all the spectra of Fig. 7A, the ratios of the integrated intensities of the D and G bands were obtained. The ratio of the integrated intensities of the D and G bands has been used to estimate the in-plane graphite crystalline length ( $L_a$ ) [66] and is commonplace in the analysis of Raman spectra for graphitic carbons [37]. Cuesta et al. [67] have demonstrated the limitations in the direct application using D and G bands ratios to estimate for  $L_a$  since relative errors  $\approx 100\%$  have been seen with heavily disordered carbons. Nevertheless, the ratio is still a useful diagnostic tool for following the increase in disorder in N-CNTs with increasing nitrogen content as shown in Fig. 7B. A linear increase in the ratio of integrated intensities with nitrogen doping suggests that the edge plane density increases, i.e., shorter  $L_a$ , in more heavily doped N-CNTs. For N-CNTs with 9.7 at.% nitrogen content,  $L_a$  is about five times smaller than for non-doped CNTs.

### 3.4. Iodimetric titration

Pyridinic surface functionalities on carbons can act as Bronsted–Lowry bases and consequently exist as positively charged moieties when protonated [51]. The estimation of surface  $pK_A$  values for polar surfaces is commonly referred

to as the  $\text{pH}_{\text{pzc}}$  [68]. For traditional graphitic materials,  $\text{pH}_{\text{pzc}}$  values are typically near or below 7, dictated by acidic oxygen functionalities imparted from exposure to ambient conditions and/or from oxidative preparation steps. We demonstrated previously that N-CNTs doped with 4.0 at.% nitrogen possess a much more alkaline  $\text{pH}_{\text{pzc}}$  value of  $9.3 \pm 0.3$  due to the prevalence of positively charged nitrogen functionalities [33]. We determined that the positive surface charge of N-CNTs at neutral pH from the more basic Bronsted–Lowry character imbued distinct electrochemical behavior. For example, the observed oxidation rate constant of dihydroxyphenylacetic acid (DOPAC), an anionic catecholamine, is two orders of magnitude greater at N-CNT film electrodes than at non-doped varieties because of a favorable ionic attraction [33].

The reductive character of graphitic carbons, may also be influenced by nitrogen doping. Strelko et al. [69] and Boehm et al. [8] have reported that nitrogenated graphitic carbons exhibit increased electron donating demonstrated by the reductive gas phase adsorption of molecular oxygen. More recently, Nevidomskyy et al. [4] predicted that nitrogen doping in carbon nanotubes will result in chemically active, localized areas of higher electron density. We also have observed that oxygen adsorption at N-CNTs is facile and promotes the electrocatalysis of oxygen in aqueous solutions [32]. We believe that the increased electron density of N-doped CNTs has a strong influence on catalytic activity observed [8]. To assess this, an iodimetric analysis was employed as described by Oliveira et al. [38]. Oliveira et al. estimated the relative number of reducing sites of thermally activated carbons (AC) by measuring the consumed equivalents of iodine in a suspension of AC and  $\text{I}_3^-$ . Interaction of  $\text{I}_3^-$  with reducing surface sites on AC catalyzed the reduction of  $\text{I}_3^-$  to  $\text{I}^-$ . Fig. 8 shows preliminary results of iodimetric analysis on various N-CNTs containing increasing amounts of nitrogen. A direct correlation between nitrogen content and the number of reducing sites is apparent, with triple the number of active sites observed for N-CNTs containing 7.5 at.% nitrogen over non-doped CNTs. The increase in reductive character of more heavily doped N-CNTs moderately follows the rise in the amount

of nitrogen coordinated as pyridinic-like functionalities as discussed above and illustrated in Fig. 8B. Attempts to correlate enhancements in chemical reactivity with nitrogen doping have been reported previously. For instance, Szymanski et al. [70] noted an increase in the basicity of  $\text{NH}_3$ -treated activated carbons tracks with the increase in the amount of pyridinic-type nitrogen. Boehm et al. [8] hypothesized that the increased activity for oxidative reactions of activated carbon tracked with the increase in pyridinic nitrogen functionalities, but they were not able to directly correlate its influence. At this juncture is not possible to discern the specific role of nitrogen on the enhancement of the electron donating character of nitrogenated carbons. However, the plausibility of pyridinic nitrogen's importance is supported by the availability of the extra lone pair of electrons on the nitrogen atom, which increases electron density on graphitic edge planes. It is reasonable to expect that edge planes, which are commonly known to be reactive sites, will show increased reactivity due to electron density garnered from incorporation of nitrogen in pyridinic-like coordination.

#### 4. Conclusions

A method for the selective doping of CNTs containing 0–10 at.% nitrogen based on a modified floating catalyst CVD methodology utilizing  $\text{NH}_3$  was described. The fraction of  $\text{NH}_3$  in the carrier gas feed stream used during CNT growth is seen to be directly proportional to the incorporated nitrogen levels. The structural and compositional features of N-CNTs containing various amounts of nitrogen were reported. Changes in XPS and Raman signatures are used to estimate the degree of structural disorder and nitrogen content. Iodimetry results showed that larger equivalents of were neutralized with N-CNTs suggesting that the reductive character increases with the increase in nitrogen content. The reported methodology for the regulated growth and selective nitrogen doping of CNTs opens up new ways to systematically study the influence of nano-carbon composition and structure on chemical and electrochemical reactivity in a host of applications.

#### Acknowledgements

Financial support of this work was provided in part by the R.A. Welch Foundation (Grant F-1529), NSF (grant CHE-0134884) and the Strategic Partnership for Research in Nanotechnology (SPRING). We also acknowledge the NSF MRI program (grant CHE-0216443) for acquisition of the Raman Microprobe. S.M. acknowledges the Harrington Foundation and the NSF for fellowship support.

#### References

- [1] Endo M, Hayashi T, Hong SH, Enoki T, Dresselhaus MS. Scanning tunneling microscope study of boron-doped highly oriented pyrolytic graphite. *J Appl Phys* 2001;90(11):5670–4.

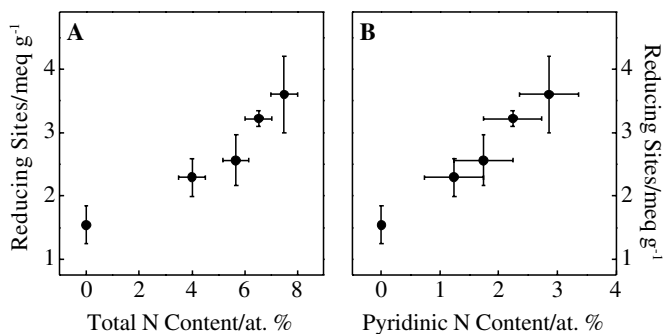


Fig. 8. Plot of number of reducing sites ( $\text{meq g}^{-1}$ ) versus (A) total nitrogen content and (B) pyridinic nitrogen in N-CNTs.

- [2] Glenis S, Nelson AJ, Labes MM. Sulfur doped graphite prepared via arc discharge of carbon rods in the presence of thiophenes. *J Appl Phys* 1999;86(8):4464–6.
- [3] Kim DP, Lin CL, Mihalisin T, Heiney P, Labes MM. Electronic properties of nitrogen-doped graphite flakes. *Chem Mater* 1991;3(4):686–92.
- [4] Nevidomskyy AH, Csanyi G, Payne MC. Chemically active substitutional nitrogen impurity in carbon nanotubes. *Phys Rev Lett* 2003;91(10):1055021–25.
- [5] dos Santos MC, Alvarez F. Nitrogen substitution of carbon in graphite: structure evolution toward molecular forms. *Phys Rev B* 1998;58(20):13918–24.
- [6] Sjoström H, Stafström S, Boman M, Sundgren JE. Superhard and elastic carbon nitride thin-films having fullerene-like microstructure. *Phys Rev Lett* 1995;75(7):1336–9.
- [7] Lahaye J, Nanse G, Bagreev A, Strelko V. Porous structure and surface chemistry of nitrogen containing carbons from polymers. *Carbon* 1999;37(4):585–90.
- [8] Stohr B, Boehm HP, Schlögl R. Enhancement of the catalytic activity of activated carbons in oxidation reactions by thermal-treatment with ammonia or hydrogen-cyanide and observation of a superoxide species as a possible intermediate. *Carbon* 1991;29(6):707–20.
- [9] Mangun CL, Benak KR, Economy J, Foster KL. Surface chemistry, pore sizes and adsorption properties of activated carbon fibers and precursors treated with ammonia. *Carbon* 2001;39:1809–20.
- [10] Bashkova S, Bagreev A, Bandosz TJ. Adsorption/oxidation of CH<sub>3</sub>SH on activated carbons containing nitrogen. *Langmuir* 2003;19(15):6115–21.
- [11] Boehm HP, Mair G, Stoehr T, Derincon AR, Tereczki B. Carbon as a catalyst in oxidation reactions and hydrogen halide elimination-reactions. *Fuel* 1984;63(8):1061–3.
- [12] Boehm HP, Derincon AR, Stohr T, Tereczki B, Vass A. Activation of carbon catalysts for oxidation reactions by treatment with ammonia or hydrogen-cyanide, and possible causes for the loss of activity during catalytic action. *J Chimie Phys Phys-Chimie Biol* 1987;84(11–12):1449–55.
- [13] Mang D, Boehm HP, Stanczyk K, Marsh H. Inhibiting effect of incorporated nitrogen on the oxidation of microcrystalline carbons. *Carbon* 1992;30(3):391–8.
- [14] Mrha J. Study of catalysts for fuel cell electrodes IV. Active carbon electrodes for oxygen in alkaline electrolyte. *Collect Czech Chem Commun* 1967;32(2):708–19.
- [15] Kublanovsii VS, Oblovatnaya SY. Catalytic activity of synthetic nitrogen-containing coals for the hydrogen peroxide decomposition reaction. *Ukrainian Chem J* 2000;66(1):18–20.
- [16] Kinoshita K. Carbon: electrochemical and physicochemical properties. New York: John Wiley and Sons, Inc.; 1988, p. 1–85.
- [17] Inagaki M, Radovic LR. Nanocarbons. *Carbon* 2002;40(12):2279–82.
- [18] Belz T, Sanchez E, Yang J, Schoonmaker R, Sauer H, Find J, et al. Fullerene-like nanocarbons: application potentials in heterogeneous reactions. In: *Proceedings—Electrochemical Society, Recent advances in the chemistry and physics of fullerenes and related materials*, 98–8, 1998, p. 169–80.
- [19] Sanchez E, Yang Y, Find J, Braun T, Schoonmaker R, Belz T, et al. Elemental carbon as catalytic material: recent trends and perspectives. *Sci Technol Catal* 1998–1999:121317–26.
- [20] Subramoney S. Novel nanocarbons—Structure, properties, and potential applications. *Adv Mater* 1998;10(15):1157–71.
- [21] Sen R, Satishkumar BC, Govindaraj S, Harikumar KR, Rengathanan MK, Rao CNR. Nitrogen-containing carbon nanotubes. *J Mater Chem* 1997;7(12):2335–7.
- [22] Yudasaka M, Kikuchi R, Ohki Y, Yoshimura S. Nitrogen-containing carbon nanotube growth from Ni phthalocyanine by chemical vapor deposition. *Carbon* 1997;35(2):195–201.
- [23] Terrones M, Terrones H, Grobert N, Hsu WK, Zhu YQ, Hare JP, et al. Efficient route to large arrays of CN<sub>x</sub> nanofibers by pyrolysis of ferrocene/melamine mixtures. *Appl Phys Lett* 1999;75(25):3932–4.
- [24] Nath M, Satishkumar BC, Govindaraj A, Vinod CP, Rao CNR. Production of bundles of aligned carbon and carbon–nitrogen nanotubes by the pyrolysis of precursors on silica-supported iron and cobalt catalysts. *Chem Phys Lett* 2000;322(5):333–40.
- [25] Droppa R, Hammer P, Carvalho ACM, dos Santos MC, Alvarez F. Incorporation of nitrogen in carbon nanotubes. *J Non-Crystal Solids* 2002;299(2):874–9.
- [26] Lee CJ, Lyu SC, Kim HW, Lee JH, Cho KI. Synthesis of bamboo-shaped carbon–nitrogen nanotubes using C<sub>2</sub>H<sub>2</sub>–NH<sub>3</sub>–Fe(CO)<sub>5</sub>(CO)<sub>5</sub> system. *Chem Phys Lett* 2002;359(1–2):115–20.
- [27] Webster S, Maultzsch J, Thomsen C, Liu J, Czerw R, Terrones M, et al. Raman characterization of nitrogen doped multiwalled carbon nanotubes. *Mater Res Soc Symp Proc* 2003;772(M):M781–6.
- [28] Maldonado S, Stevenson KJ. Direct preparation of carbon nanofiber electrodes via pyrolysis of iron(II) phthalocyanine: electrocatalytic aspects for oxygen reduction. *J Phys Chem B* 2004;108(31):11375–83.
- [29] Jang JW, Lee CE, Lyu SC, Lee TJ, Lee CJ. Structural study of nitrogen-doping effects in bamboo-shaped multiwalled carbon nanotubes. *Appl Phys Lett* 2004;84(15):2877–9.
- [30] Blase X, Charlier JC, De Vita A, Car R, Redlich P, Terrones M, et al. Boron-mediated growth of long helicity-selected carbon nanotubes. *Phys Rev Lett* 1999;83(24):5078–81.
- [31] Redlich P, Loeffler J, Ajayan PM, Bill J, Aldinger F, Ruhle M. B–C–N nanotubes and boron doping of carbon nanotubes. *Chem Phys Lett* 1996;260(3–4):465–70.
- [32] Maldonado S, Stevenson KJ. Influence of nitrogen doping on oxygen reduction electrocatalysis at carbon nanofiber electrodes. *J Phys Chem B* 2005;109(10):4707–16.
- [33] Maldonado S, Morin S, Stevenson KJ. Electrochemical oxidation of catecholamines and catechols at carbon nanotube electrodes. *The Analyst*, in press.
- [34] Endo M. Grow carbon fibers in the vapor phase. *Chemtech* 1988;18(9):568.
- [35] Kim TY, Lee KR, Eun KY, Oh KH. Carbon nanotube growth enhanced by nitrogen incorporation. *Chem Phys Lett* 2003;372(4):603–7.
- [36] Marquadt DW. An algorithm for least squares estimation of nonlinear parameters. *J Soc Ind Appl Math* 1963;11(2):431–41.
- [37] Cuesta A, Dhamelincourt P, Laureyns J, Martinezalonso A, Tascon JMD. Raman microprobe studies on carbon materials. *Carbon* 1994;32(8):1523–32.
- [38] Oliveira LCA, Silva CN, Yoshida MI, Lago RM. The effect of H<sub>2</sub> treatment on the activity of activated carbon for the oxidation of organic contaminants in water and the H<sub>2</sub>O<sub>2</sub> decomposition. *Carbon* 2004;42(11):2279–84.
- [39] Lee YT, Kim NS, Bae SY, Park J, Yu SC, Ryu H, et al. Growth of vertically aligned nitrogen-doped carbon nanotubes: Control of the nitrogen content over the temperature range 900–1100 °C. *J Phys Chem B* 2003;107(47):12958–63.
- [40] McCreery RL. Carbon electrodes: structural effects on electron transfer kinetics. In: Bard AJ, editor. *Carbon electrodes: structural effects on electron transfer kinetics*. New York: Dekker; 1991. p. 268–73.
- [41] Papakonstantinou P, Lemoine P. Influence of nitrogen on the structure and nanomechanical properties of pulsed laser deposited tetrahedral amorphous carbon. *J Phys—Condens Matter* 2001;13(13):2971–87.
- [42] Kamau GN, Willis WS, Rusling JF. Electrochemical and electron spectroscopic studies of highly polished glassy carbon electrodes. *Anal Chem* 1985;57(2):545–51.
- [43] Cabaniss GE, Diamantis AA, Murphy WR, Linton RW, Meyer TJ. Electrocatalysis of proton-coupled electron-transfer reactions at glassy-carbon electrodes. *J Am Chem Soc* 1985;107(7):1845–53.
- [44] Estrade-Szwarckopf H. XPS photoemission in carbonaceous materials: a “defect” peak beside the graphitic asymmetric peak. *Carbon* 2004;42(8–9):1713–21.

- [45] Leiro JA, Heinonen MH, Laiho T, Batirev IG. Core-level XPS spectra of fullerene, highly oriented pyrolytic graphite, and glassy carbon. *J Electron Spectrosc Relat Phenom* 2003;128(2–3):205–13.
- [46] Sette F, Wertheim GK, Ma Y, Meigs G. Lifetime and screening of the C 1s photoemission in graphite. *Phys Rev B* 1990;41(14):9766–70.
- [47] Terrones M, Ajayan PM, Banhart F, Blase X, Carroll DL, Charlier JC, et al. N-doping and coalescence of carbon nanotubes: synthesis and electronic properties. *Appl Phys A—Mater Sci Process* 2002;74(3):355–61.
- [48] Wei J. Formation of b-C<sub>3</sub>N<sub>4</sub> crystals at low temperature. *J Appl Phys* 2001;89(7):4099–104.
- [49] Kuper CA, Labes MM. A new method of doping pyrolytic graphite utilizing laser heating in the presence of organic heteroatomic vapors. *Chem Mater* 1999;11(2):408–11.
- [50] Muhl S, Mendez JM. A review of the preparation of carbon nitride films. *Diamond Relat Mater* 1999;8(10):1809–30.
- [51] Pels JR, Kapteijn F, Moulijn JA, Zhu Q, Thomas KM. Evolution of nitrogen functionalities in carbonaceous materials during pyrolysis. *Carbon* 1995;33(11):1641–53.
- [52] Casanovas J, Ricart JM, Rubio J, Illas F, JimenezMateos JM. Origin of the large N 1s binding energy in X-ray photoelectron spectra of calcined carbonaceous materials. *J Am Chem Soc* 1996;118(34):8071–6.
- [53] Biniak S, Szymanski G, Siedlewski J, Swiatkowski A. The characterization of activated carbons with oxygen and nitrogen surface groups. *Carbon* 1997;35(12):1799–810.
- [54] Choi HC, Park J, Kim B. Distribution and structure of N atoms in multiwalled carbon nanotubes using variable-energy X-ray photoelectron spectroscopy. *J Phys Chem B* 2005;109(10):4333–40.
- [55] Bjorneholm O, Nilsson A, Sandell A, Hernnas B, Martensson N. Determination of time scales for charge transfer screening in physisorbed molecules. *Phys Rev Lett* 1992;68(12):1892–5.
- [56] Soto G. Electron spectroscopic identification of carbon species on CN<sub>x</sub> films. *Mater Lett* 2001;49(6):352–6.
- [57] Angoni K. Remarks on the structure of carbon materials on the basis of Raman spectra. *Carbon* 1993;31(4):537–47.
- [58] Riedo E, Comin F, Chevrier J, Schmithusen F, Decossas S, Sancrotti M. Structural properties and surface morphology of laser-deposited amorphous carbon and carbon nitride films. *Surf Coat Technol* 2000;125(1–3):124–8.
- [59] Ronning C, Feldermann H, Merk R, Hofsass H, Reinke P, Thiele JU. Carbon nitride deposited using energetic species: a review on XPS studies. *Phys Rev B* 1998;58(4):2207–15.
- [60] Choi S, Park KH, Lee S, Koh KH. Raman spectra of nano-structured carbon films synthesized using ammonia-containing feed gas. *J Appl Phys* 2002;92(7):4007–11.
- [61] Darmstadt H, Summchen L, Ting JM, Roland U, Kaliaguine S, Roy C. Effects of surface treatment on the bulk chemistry and structure of vapor grown carbon fibers. *Carbon* 1997;35(10–11):1581–5.
- [62] Bonhomme F, Lassegues JC, Servant L. Raman spectroelectrochemistry of a carbon supercapacitor. *J Electrochem Soc* 2001;148(11):E450–8.
- [63] Nemanich RJ, Solin SA. First-order and second-order Raman scattering from finite-size crystals of graphite. *Phys Rev B* 1979;20(2):392–401.
- [64] Wang Y, Alsmeyer DC, McCreery RL. Raman-spectroscopy of carbon materials—structural basis of observed spectra. *Chem Mater* 1990;2(5):557–63.
- [65] Rouzaud JN, Oberlin A, Beny-Bassez C. Relationship model between optical-properties and crystalline organization of carbonaceous materials—the carbon-films. *Comptes Rendus L Acad Des Sci Ser II* 1983;296(5):369–72.
- [66] Tuinstra F, Koenig JL. Raman spectrum of graphite. *J Chem Phys* 1970;53(3):1126–30.
- [67] Cuesta A, Dhamelincourt P, Laureyns J, Martinez-Alonso A, Tascon JMD. Comparative performance of X-ray diffraction and Raman microprobe techniques for the study of carbon materials. *J Mater Chem* 1998;8(12):2875–9.
- [68] Chen WF, Cannon FS, Rangel-Mendez JR. Ammonia-tailoring of GAC to enhance perchlorate removal. I: Characterization of NH<sub>3</sub> thermally tailored GACs. *Carbon* 2005;43(3):573–80.
- [69] Strelko VV, Kuts VS, Thrower PA. On the mechanism of possible influence of heteroatoms of nitrogen, boron and phosphorus in a carbon matrix on the catalytic activity of carbons in electron transfer reactions. *Carbon* 2000;38(10):1499–503.
- [70] Szymanski G, Grzybek T, Papp H. Influence of nitrogen surface functionalities on the catalytic activity of activated carbon in low temperature SCR of NO<sub>x</sub> with NH<sub>3</sub>. *Catal Today* 2004;90(1): 51–9.